

Design and Analysis of a Stewart-Platform-Based Six-Axis Load Cell

by

Maria Rosa Ruiz

Submitted to the Department of Mechanical Engineering
in partial fulfillment of the requirements for the degree of

Bachelor of Science in Mechanical Engineering

at the

MASSACHUSETTS INSTITUTE OF TECHNOLOGY

June 2017

© Massachusetts Institute of Technology 2017. All rights reserved.

Author
Department of Mechanical Engineering
May 17, 2017

Certified by
H. Harry Asada
Ford Professor of Engineering
Thesis Supervisor

Accepted by
Rohit Karnik
Associate Professor of Mechanical Engineering
Undergraduate Officer

Design and Analysis of a Stewart-Platform-Based Six-Axis Load Cell

by

Maria Rosa Ruiz

Submitted to the Department of Mechanical Engineering
on May 17, 2017, in partial fulfillment of the
requirements for the degree of
Bachelor of Science in Mechanical Engineering

Abstract

In this work, a six-axis load cell based on the geometry of a Stewart platform was developed. Its geometry and functional requirements were motivated by the needs of robotic limbs designed to be attached to human workers to support them in typically unergonomic positions. The sensor can measure forces and torques in six degrees of freedom, and can stably support the worker in various hanging positions while still being sensitive to load measurements in different directions. Furthermore, it is made from inexpensive, commonly available cantilever beam load cells. In the least accurate direction, M_x , our measurements were consistently 20% below the nominal applied load. In the most accurate directions, F_x , M_y , and M_z , our measurements were consistently within 5% of the nominal applied loads. Performance can be optimized using the condition number of the transformation matrix. The full-scale version of the hex sensor is also designed and optimized based on its condition number.

Thesis Supervisor: H. Harry Asada
Title: Ford Professor of Engineering

Acknowledgments

I would like to thank Daniel Gonzalez for being willing to share his impressive amounts of mechanical engineering knowledge and for being the best mentor I could ask for, Prof. Harry Asada for his advice and the opportunity to discover robotics research, and Dr. Barbara Hughey for her help with data analysis and for introducing MIT and mechanical engineering to me. I would also like to thank my parents and siblings for their love and encouragement (and financial support), as well as Kath Xu, Melody Liu, and all my friends for their unfailing confidence in me.

Contents

1	Motivation	13
1.1	Proposal: Extra Robotic Limbs (XRL)	14
1.2	Sensing Between Robot and Human	15
2	Design of Small Hex Sensor	17
2.1	Functional Requirements	17
2.2	Design Process	18
2.3	Joint Design	20
2.4	Calculating Forces and Torques	20
3	Measurement and Testing	25
4	Results and Analysis	27
4.1	Measured Values Compared to Actual Values	27
4.2	Noise	28
4.3	Sources of Error	30
4.3.1	Performance Analysis	30
5	Preliminary Work on Full-Size Hex Sensor	33
5.1	Harness Selection	33
5.2	Joint Design	34
5.3	Geometry Optimization	35
5.4	Solid Model of Full Scale Hex Sensor	39

List of Figures

1-1	Example of personal protective equipment, including SCBA system, worn at the Fukushima site.	14
1-2	The XRL in centaur mode, following behind a walking human; the XRL in mantis mode, supporting the human doing work on the ground; and the XRL in sitting mode, supporting the human like a chair.	15
2-1	Commercially available six-axis load cell. It costs \$4300, and has a constant accuracy of 3% full scale and a repeatability of 0.133N, or 0.067% full scale.	17
2-2	A typical Stewart platform, where the prismatic joints in the legs give the top platform six degrees of freedom of motion.	18
2-3	The total forces and moments on the load cell in the S-beam configuration on the left are the same as if it were loaded conventionally, as shown on the left ($F = 0$ and $M_{sense} = FL$); therefore, there is no parasitic loading to distort the readings.	19
2-4	The small hex sensor's legs and platform before assembly, and the completed hex sensor.	20
2-5	Each leg reports an axial force, N_n	21
2-6	Relevant angles and distances that determine overall geometry	21
2-7	For each pair of legs, the effective forces and moment at the top of the triangle can be calculated.	22

2-8	The effective forces and moment at the top of each pair of legs can be transformed again into the effective loads and torques applied at the center of the top platform.	23
3-1	Test setup: the hex sensor was held in various orientations and known weights hung from the sensor to test accuracy and repeatability. . . .	26
4-1	Sample plot of measured moment plotted against actual applied moment. The fit is linear and represents the proportional accuracy of the measurement in this particular direction.	28
4-2	Signal readings after hex sensor was preloaded with 1kg and then zeroed; the noise range is about +/-0.03kg, or 1.1% FS. Power spectrum for the signal: signal-to-noise ratio is roughly 30 dB.	29
5-1	To test rescue harness comfort, a subject was suspended from the ceiling by three attachment points (circled in red) and comfort—especially how the harness dug into the subject's body—was noted.	34
5-2	The Yates Voyager 380 rescue harness	34
5-3	A typical D-ring on a rescue harness. The D-ring has three degrees of freedom and can be approximated as a ball joint.	35
5-4	Each pair of legs needs to constrain a total of 14 degrees of freedom, and the ball joint from the harness attachment point constrained three of these. Two options for joint combinations are displayed; the ball joint and pin joint combination was chosen.	35
5-5	The six attachment points of each triangular pair of FSHS legs on the XRL platform were the design parameters varied in the search for the lowest condition number.	36
5-6	\mathbb{H}_1 breaks down axial forces into their x , y , and z components.	37
5-7	Example plot of condition number; used as part of hill-climbing minimization.	38
5-8	Diagram of optimal FSHS geometry	39

5-9	Leg design	39
5-10	Pair of legs	40
5-11	Solid model of proposed full-size hex sensor	40
6-1	Load lifters are common hiking pack features that transfer weight from the shoulders to the hips.	42
6-2	The Second Spine can either be loose and flexible, or, when, pulled into compression, rigid and load-bearing.	42

Chapter 1

Motivation

From cleaning up reactor meltdowns and former weapons production sites to regular maintenance at nuclear power plants, nuclear site work requires hundreds of hours of manual labor. Workers at both cleanup sites and normally operating power plants complete a wide variety of tasks: at cleanup sites, they patch leaks and lay piping to direct cooling water; during outages, they replace fuel and update equipment [1][6][7].

However, workers can only stay at the site for short time periods. Their personal protective equipment, which must include a self-contained breathing apparatus (SCBA) and layers of stifling clothing, is bulky and heavy, making it difficult to maneuver within the site and speeding up fatigue (see Figure 1-1). Because it lacks a cooling system, the suit quickly becomes uncomfortably hot. Furthermore, workers are limited by their air supply—even a 60-minute supply may yield only 15 minutes of work time after exhaustion and time for decontamination steps are factored in [2]. Both outages and cleanup efforts are extremely expensive—outages, for example, last an average of 35 days, cost the government millions, and force residents to pay more to use conventionally-produced electricity. Improving the conditions for workers in hazmat suits by increasing comfort and mobility will improve their work efficiency, leading to cost savings.



Figure 1-1: Example of personal protective equipment, including SCBA system, worn at the Fukushima site.

1.1 Proposal: Extra Robotic Limbs (XRL)

A pair of extra robotic limbs (XRL) is proposed. They will be attached to the worker via a harness, and follow behind in “centaur” mode, moving based on the actions of the human worker. The extra limbs will be able to support the SCBA system—allowing for more stored air—as well as a cooling system, increasing the overall stay time.

In addition, the XRL can support the worker in a variety of positions difficult to maintain on one's own. In the “sitting” mode, the XRL will stiffen so the worker can sit hanging from the harness. In the “mantis” mode, the XRL will bend to support the worker doing tasks close to the ground, relieving the pressure on the worker's knees. This extra support will increase the amount of time a worker can spend in uncomfortable positions, improving their range of motion. The three modes are shown in Figure 1-2.

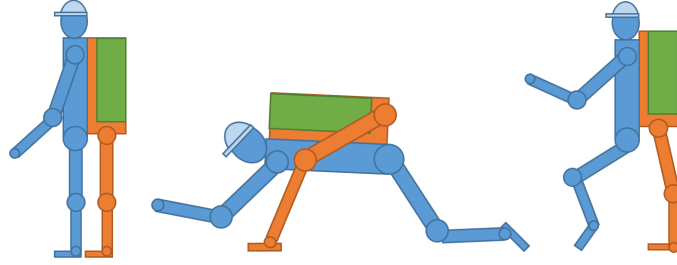


Figure 1-2: The XRL in centaur mode, following behind a walking human; the XRL in mantis mode, supporting the human doing work on the ground; and the XRL in sitting mode, supporting the human like a chair.

1.2 Sensing Between Robot and Human

The XRL will gather information about the worker's movements and the positions of their limbs through a combination of a stereo camera on the worker's head for simultaneous location and mapping and inertial measurement units (IMUs) on the worker's limbs to capture body kinematics. There will also be a six axis force/torque sensor at the attachment between robot and human. Although the IMUs can give the position of the human's limbs in 3D space, the force sensor is an important safety feature that gives the intentions of the operator: for example, when approaching an obstacle, a force from the operator towards the robot signals that the operator is trying to back away, and the robot can react accordingly. This thesis will focus on the development and characterization of a small prototype force sensor with similar geometry to the final force sensor, and present a figure of merit for evaluating force sensors in this configuration.

Chapter 2

Design of Small Hex Sensor

2.1 Functional Requirements

The force sensor's requirements come from its use as both sensor and means of attaching the robot to the worker. First, the force sensor must be a multi-axis sensor that measures forces and torques in six degrees of freedom. Next, the attachment must provide a stable, comfortable, and compliant connection between the robot legs and person. Currently available multi-axis load cells such as the one in Figure 2-1 are not only expensive but also have just one attachment point, which would leave the worker dangling in the sitting and mantis positions.



Figure 2-1: Commercially available six-axis load cell. It costs \$4300, and has a constant accuracy of 3% full scale and a repeatability of 0.133N, or 0.067% full scale.

2.2 Design Process

A small, proof-of-concept version of the hex sensor (as the force sensor will now be referred to) was designed to explore the geometry and method of sensing. Because the attachment serves as both strap and sensor, the geometry of the attachment must provide enough information to calculate all forces and torques between two platforms using only axial force measurements along the connecting legs, and the area of connection between the loading point and the base of the sensor must be large to provide stability. A Stewart platform, shown in Figure 2-2, has a similar function, providing six degrees of freedom of motion with only linear actuators while supporting a platform. For the hex sensor, individual load cells were integrated into beams placed into a hexapod configuration connecting two platforms: one representing the harness attached to the person, and the other the robot.

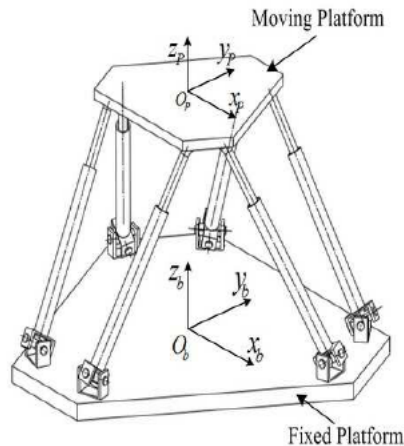


Figure 2-2: A typical Stewart platform, where the prismatic joints in the legs give the top platform six degrees of freedom of motion.

Next, different combinations of sensors and materials were considered for the legs, which needed to measure forces applied axially. Either forces could be measured directly, or measured strains could be combined with stiffness data to calculate force. Possibilities for the legs included high-shore, preloaded stretch sensors; high-shore rubber with strain gauges; and load cells. The stretch sensors recovered too slowly after being stretched to be practical for a real-time application. Strain sensors cannot withstand the strains on even the highest shore rubber. Load cells were chosen

because they were robust, accurate, and could be used in series with rubber for a more compliant sensor.

For this hex sensor, 1-kg cantilever beam load cells were used, along with a Phidgets 4-Input bridge amplifier. Using the beam in an S-beam configuration allowed forces to be measured in a straight line through the leg. Figure 2-3 shows how the loading in the S-beam configuration is the same as when the load cell is loaded conventionally.

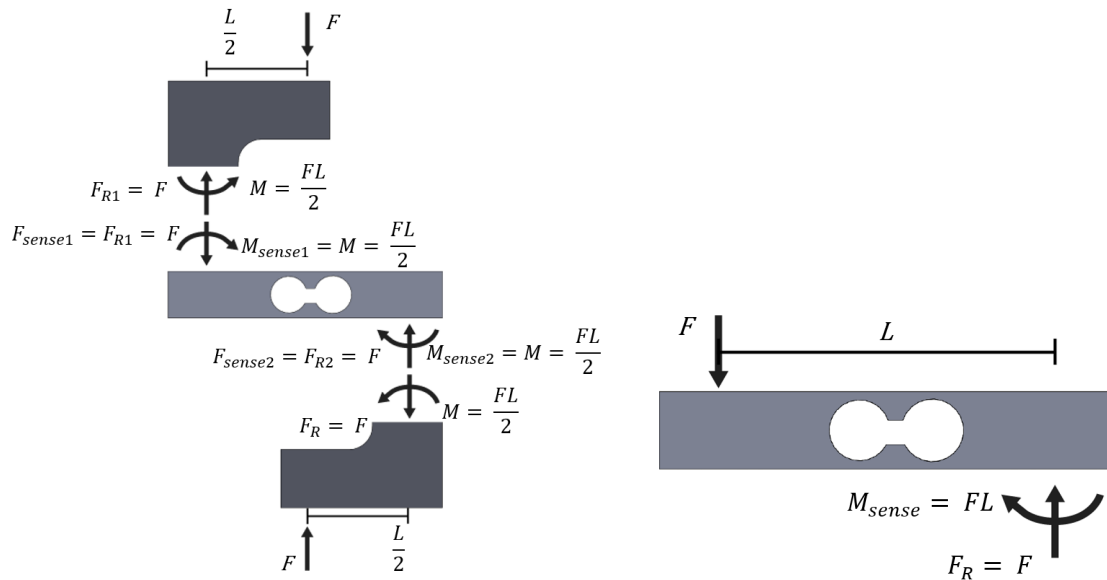


Figure 2-3: The total forces and moments on the load cell in the S-beam configuration on the left are the same as if it were loaded conventionally, as shown on the right ($F = 0$ and $M_{sense} = FL$); therefore, there is no parasitic loading to distort the readings.

Each load cell was calibrated by assembling the leg, hanging 3 known weights off each leg, and then finding a calibration constant A from the results such that $force = A * voltage$.

2.3 Joint Design

The joints connecting the legs to each platform had to be chosen to fully constrain the two platforms. Using the 3D version of Gruebler's equation,

$$D.O.F. = 6(N - 1) - 5P_5 - 4P_4 - 3P_3 - 2P_2 - 1P_1 \quad (2.1)$$

where P_n represents the number of pairs that block n degrees of freedom, we can calculate that to end up with 0 degrees of freedom for an 8-part mechanism made from 6 beams and 2 plates, we need to constrain 42 degrees of freedom. For simplicity and ease of manufacturing, and to ensure that the forces were transmitted purely axially through the leg, 12 ball joints were used, so $P_3 = 12$. The miniature hexapod is left with 6 degrees of freedom, because each leg can spin in place, but the rotation of each leg does not have a statistically significant effect on the measurement. The ball joints were 3D printed.



Figure 2-4: The small hex sensor's legs and platform before assembly, and the completed hex sensor.

2.4 Calculating Forces and Torques

The geometry of the hex sensor can be used to calculate the effective forces and torques at the center of the platform representing the robot from the axial forces felt by each leg, shown in Figure 2-5. The axial forces are read in as a matrix, N .

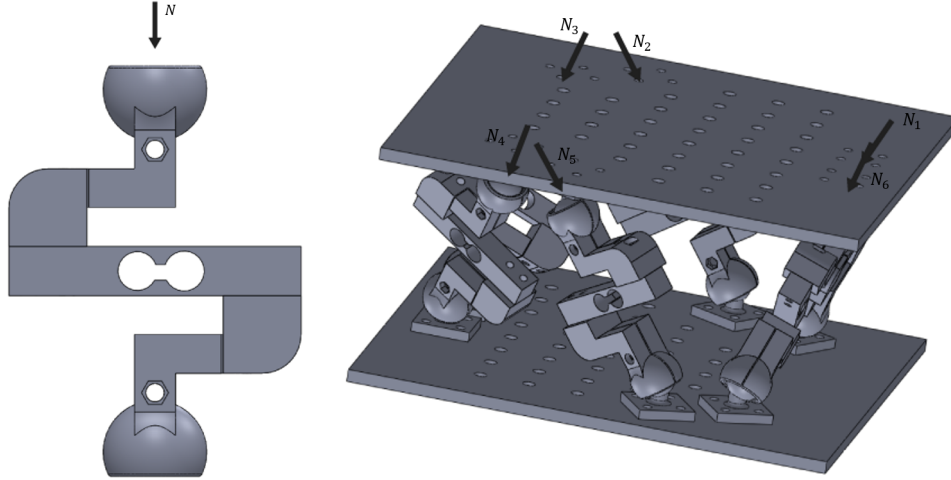


Figure 2-5: Each leg reports an axial force, N_n

$$N = \begin{pmatrix} N_1 & N_2 & N_3 & N_4 & N_5 & N_6 \end{pmatrix}^T \quad (2.2)$$

The overall geometry is determined by the angles between the legs, and their distance from the center of the platform, as shown in Figure 2-6.

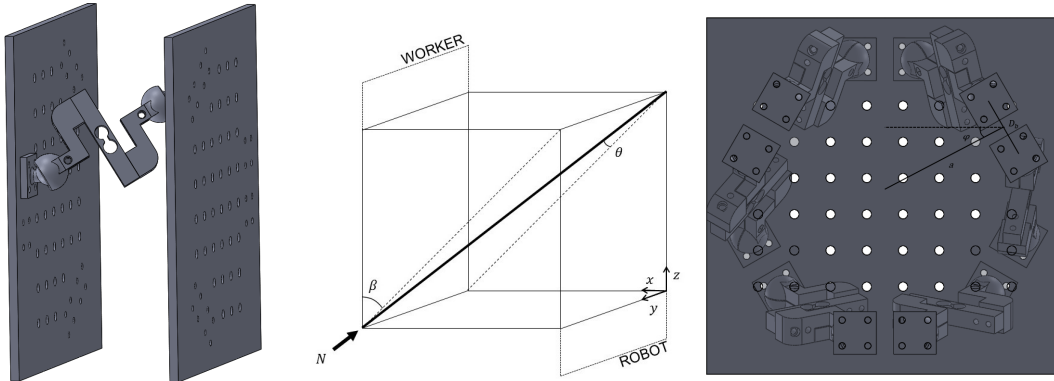


Figure 2-6: Relevant angles and distances that determine overall geometry

First, we will focus on one pair of legs. The forces felt by these legs are represented by

$$N_a = \begin{pmatrix} N_1 & N_2 \end{pmatrix}^T \quad (2.3)$$

A transformation matrix, \mathbb{J}_a , converts the forces felt in the pair of load cells to the effective forces and moments felt at the top of the triangle formed by the pair, as shown in Figure 2-7. M_z is the only direction of moment that can be distinguished

when given axial forces in a plane.

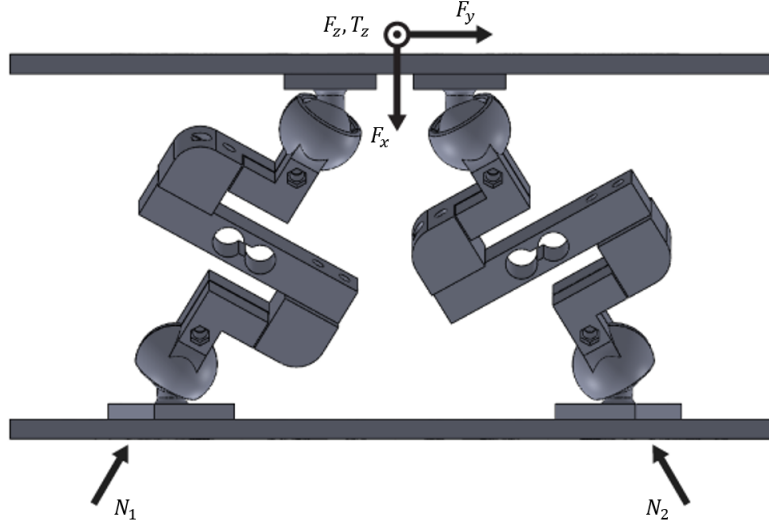


Figure 2-7: For each pair of legs, the effective forces and moment at the top of the triangle can be calculated.

From the angles labeled in Figure 2-6, \mathbb{J}_a can be calculated:

$$\mathbb{J}_a = \begin{bmatrix} \cos(\theta) \sin(\beta) & \cos(\theta) \sin(\beta) \\ -\sin(\theta) & -\sin(\theta) \\ -\cos(\theta) \cos(\beta) & -\cos(\theta) \cos(\beta) \\ \frac{D_b}{2} \cos(\theta) \sin(\beta) & -\frac{D_b}{2} \cos(\theta) \sin(\beta) \end{bmatrix}. \quad (2.4)$$

The forces and moment at the top of each triangle are

$$F_{triangle} = \mathbb{J}_a N_a \quad (2.5)$$

where

$$F_{triangle} = \left(F_x \quad F_y \quad F_z \quad T_z \right)^T. \quad (2.6)$$

For the overall hex sensor, \mathbb{J}_1 converts all the axial forces, N from equation 2.2, into forces and moment at the top of each pair of legs, perpendicular to the platform

but parallel to the triangle's base:

$$\mathbb{J}_1 = \begin{bmatrix} \mathbb{J}_a & 0 & 0 \\ 0 & \mathbb{J}_a & 0 \\ 0 & 0 & \mathbb{J}_a \end{bmatrix} \quad (2.7)$$

This yields

$$F = \mathbb{J}_1 N \quad (2.8)$$

where

$$F = (F_{x1} \ F_{y1} \ F_{z1} \ M_{z1} \ F_{x2} \ F_{y2} \ F_{z2} \ M_{z2} \ F_{x3} \ F_{y3} \ F_{z3} \ M_{z3})^T. \quad (2.9)$$

These forces are transformed by another matrix, \mathbb{J}_2 , into the effective forces and moments at the center of the platform, represented by L .

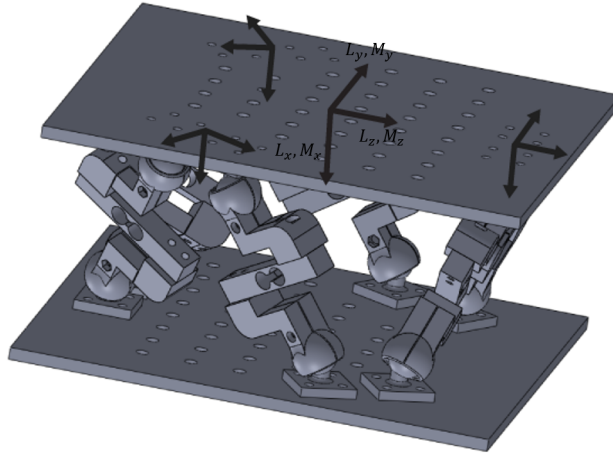


Figure 2-8: The effective forces and moment at the top of each pair of legs can be transformed again into the effective loads and torques applied at the center of the top platform.

$$\mathbb{J}_2 = \begin{bmatrix} 1 & 0 & 0 & 0 & 1 & 0 & 0 & 0 & 1 & 0 & 0 & 0 \\ 0 & 1 & 0 & 0 & 0 & -\sin(\phi) & \cos(\phi) & 0 & 0 & -\sin(\phi) & -\cos(\phi) & 0 \\ 0 & 0 & 1 & 0 & 0 & -\cos(\phi) & -\sin(\phi) & 0 & 0 & \cos(\phi) & -\sin(\phi) & 0 \\ 0 & -a & 0 & 0 & 0 & -a & 0 & 0 & 0 & -a & 0 & 0 \\ a & 0 & 0 & 0 & -a \sin(\phi) & 0 & 0 & \cos(\phi) & -a \sin(\phi) & 0 & 0 & -\cos(\phi) \\ 0 & 0 & 0 & 1 & -a \cos(\phi) & 0 & 0 & -\sin(\phi) & a \cos(\phi) & 0 & 0 & -\sin(\phi) \end{bmatrix}. \quad (2.10)$$

$$L = \mathbb{J}_2 F = \mathbb{J}_2 \mathbb{J}_1 N \quad (2.11)$$

where

$$L = \left(L_x \quad L_y \quad L_z \quad M_x \quad M_y \quad M_z \right)^T \quad (2.12)$$

at the center of the platform.

Chapter 3

Measurement and Testing

The hex sensor was tested with known weights to determine its accuracy and repeatability. To test force, a series of weights were hung under the center of the platform representing the robot. To test moment, weights were hung a known distance away from the center. The hex sensor was always preloaded with a 200g weight to decrease the effects of play within the joints. Figure 3-1 shows the measurement test setup, and the applied forces and torques are summarized in Table 3.1. The Python code zeroed the hex sensor after the preload was applied, read the cantilever load cell values, and calculated the force or moment with the transformation matrices. Forces and moments were measured in all 6 degrees of freedom, in both the positive and negative directions.

Table 3.1: Applied forces and torques during testing.

Applied forces [N]	Applied torques [N-m]
0.98	0.0622
4.90	0.3112
9.80	0.5601
-0.98	-0.0622
-4.90	-0.3112
-9.80	-0.5601

The noise in the hex sensor's readings was also measured by preloading the sensor with 1kg, zeroing it, and recording data over 10 seconds.

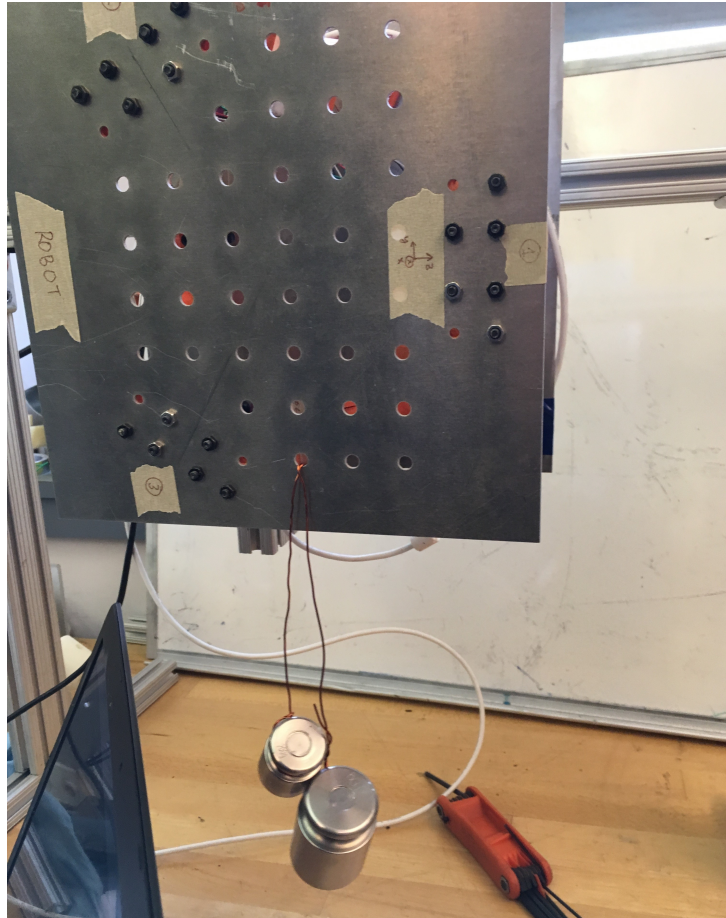


Figure 3-1: Test setup: the hex sensor was held in various orientations and known weights hung from the sensor to test accuracy and repeatability.

Chapter 4

Results and Analysis

4.1 Measured Values Compared to Actual Values

The measured force or moment (an average of 5 readings) was plotted against the actual force or moment for each degree of freedom, and a line was fit to the points using the least squares method. Figure 4-1 shows an example plot, for moment about the z axis:

To determine repeatability, the 95% confidence uncertainty in the slope was calculated. Although the intercept of the line was not always zero, the uncertainty of the intercept was greater than the value, and thus this is not a significant parameter. Accuracy was determined from the slope of the line, which was not one, signifying a proportional accuracy. For example, a slope of 0.95 corresponds to an accuracy of 5% of the nominal value. Table 4.1 shows the accuracies and repeatabilities.

Table 4.1: Proportional accuracies and repeatabilities for each direction. Results are unitless.

Direction	Proportional Accuracy	95% confidence interval over 6 measurements
L_x	0.95	0.02
L_y	0.86	0.02
L_z	0.85	0.08
M_x	0.80	0.08
M_y	0.96	0.05
M_z	1.01	0.11

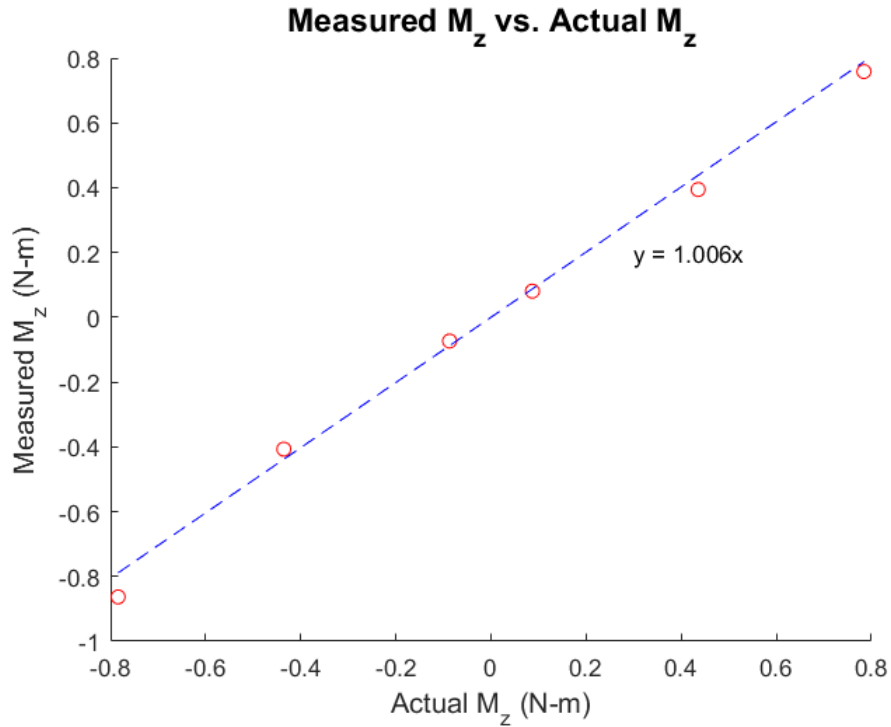


Figure 4-1: Sample plot of measured moment plotted against actual applied moment. The fit is linear and represents the proportional accuracy of the measurement in this particular direction.

Although the accuracy of the sensor was lower than desired in some directions (F_y , F_z , and M_x), the readings are linear, suggesting that the hex sensor can accurately measure changes in force and torque applied, which is what matters most for its application. Furthermore, each cantilever beam cost only \$7.00, in comparison to commercial load cells which cost thousands of dollars; for a device so much more inexpensive, it is relatively accurate.

4.2 Noise

The signal to noise ratio of the hex sensor depends on the noise measured by each individual cantilever, which in turn depends on the sampling rate—for slower sample rates, the Phidgets bridge averages the readings between outputs, resulting in less noise. For the 8-ms (125 Hz) sample rate used in this hex sensor, the preloaded and zeroed hex sensor had a signal with +/- 0.03kg of noise, or 1.1% full scale (FS).

The power spectrum for the signal was also plotted up to the Nyquist frequency, 62.5 Hz, which is the highest frequency that can be unambiguously measured. The signal-to-noise ratio is about 20 dB. The power spectrum is relatively flat, meaning there are no unwanted periodic signals corrupting the data.

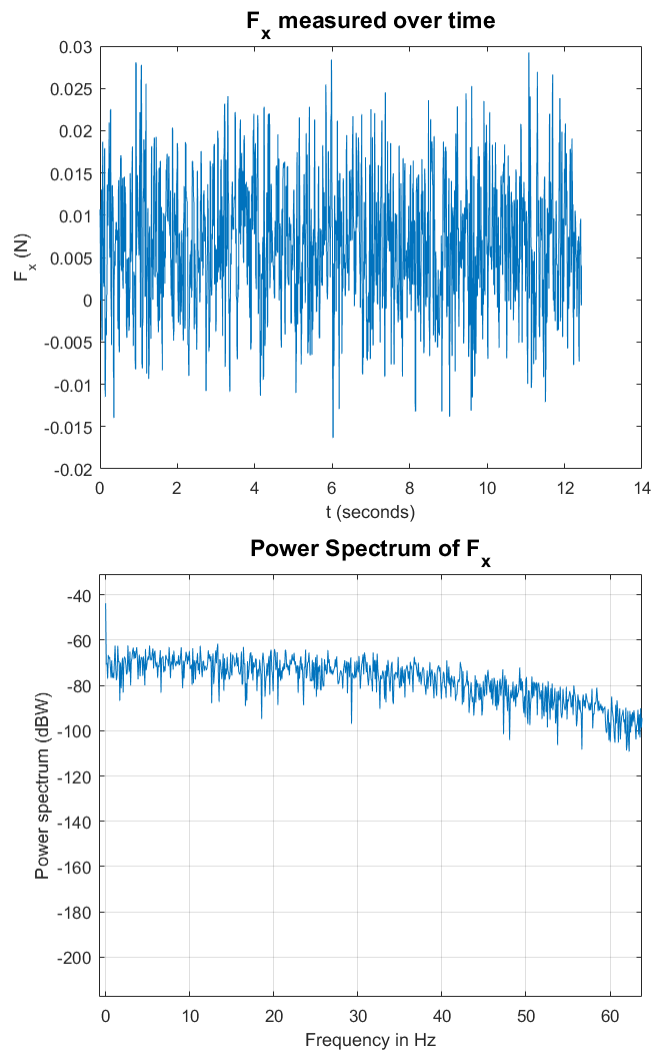


Figure 4-2: Signal readings after hex sensor was preloaded with 1kg and then zeroed; the noise range is about +/-0.03kg, or 1.1% FS. Power spectrum for the signal: signal-to-noise ratio is roughly 30 dB.

4.3 Sources of Error

First, the load cells have a repeatability error of 0.05% FS, or about 0.5g, a couple of orders of magnitude less than the measured error. Therefore, the load cells themselves cannot account for most of the measured error.

Next, to ensure that the error did not come from inaccurately assembling the hex sensor, the attachment angles were varied slightly in the code to predict the effect of errors in assembly. Even varying the angle of attachment up to an unrealistic 5 degrees did not change the output by more than 6%, suggesting that the assembly process is not responsible for most of the error.

Finally, the ball joints were 3D printed, resulting in rough surfaces within the ball joint. Furthermore, the socket assembly allowed play if not tightened enough, but compressed the ball, creating more friction, if overtightened. This could cause the load to not be perfectly axially transmitted.

4.3.1 Performance Analysis

The geometry of the hex sensor can also be analyzed to determine its effects on the sensitivity of the sensor in different directions. We can evaluate the effectiveness of the geometry through the evaluation of the overall transformation matrix \mathbb{J} :

$$\mathbb{J} = \mathbb{J}_2 \mathbb{J}_1 \tag{4.1}$$

We want the errors in the measurement of the axial forces to be magnified as little as possible by the transformation matrix [8]. For forces applied to each leg such that \mathbf{N} is a unitary matrix, the tip of the output vector of forces and moments will be inside an ellipsoid defined by the singular value decomposition of \mathbb{J} , similar to how manipulability is determined by the shape of the velocity ellipsoid.

$$\mathbb{J} = \mathbf{U} \Sigma \mathbf{V}^T \tag{4.2}$$

where \mathbf{U} and \mathbf{V} are orthogonal matrices composed of the eigenvectors of $\mathbb{J}\mathbb{J}^T$ and

$\mathbb{J}^T \mathbb{J}$, respectively, and the singular values are the values along the diagonal of Σ . For the prototype hex sensor,

$$diag(\Sigma) = (2.00 \quad 1.00 \quad 1.00 \quad 0.13 \quad 0.13 \quad 0.12). \quad (4.3)$$

However, because \mathbb{J} outputs both forces and moments, the elements of \mathbb{J} are in different units and cannot be compared (though the first three singular values can be used to compare force-measuring sensitivity, and the last three can be used for moments). We can normalize \mathbb{J} by dividing the forces and moments by the maximum expected force or moment, based on the load cell's limits [8]. In this case, $F_{max} = 51.94\text{N}$ and $M_{max} = 2.94\text{N-m}$.

$$\mathbb{J}_{norm} = \begin{bmatrix} \frac{1}{F_{max}} & 0 & 0 & 0 & 0 & 0 \\ 0 & \frac{1}{F_{max}} & 0 & 0 & 0 & 0 \\ 0 & 0 & \frac{1}{F_{max}} & 0 & 0 & 0 \\ 0 & 0 & 0 & \frac{1}{M_{max}} & 0 & 0 \\ 0 & 0 & 0 & 0 & \frac{1}{M_{max}} & 0 \\ 0 & 0 & 0 & 0 & 0 & \frac{1}{M_{max}} \end{bmatrix} \quad (4.4)$$

$$L_{norm} = \mathbb{J}_{norm} L \quad (4.5)$$

So, the normalized transformation matrix is

$$\cdot \mathbb{J}_f = \mathbb{J}_{norm} \mathbb{J} \quad (4.6)$$

$$\mathbb{J}_f = \mathbf{U}_f \Sigma_f \mathbf{V}_f^T \quad (4.7)$$

For the prototype hex sensor,

$$diag(\Sigma_f) = (0.0503 \quad 0.0503 \quad 0.0406 \quad 0.0379 \quad 0.0175 \quad 0.0175). \quad (4.8)$$

The direction of the ellipsoid's semi-major, semi-intermediate, and semi-minor

axes will be the columns of \mathbf{U} , which are linear combinations of the axial forces in each leg. The magnitudes of the axes will be the singular values. The ideal shape, a hypersphere, would signify isotropy, or equal sensitivity in all directions [4]. The condition number of a matrix, which is the ratio of the largest to smallest singular value, gives a measure of how distorted the ellipsoid is from a hypersphere. Therefore, the condition number of \mathbb{J}_f relates the relative error in the data to the relative error in the output [3]:

$$\frac{\|\delta L_{norm}\|}{\|L_{norm}\|} = cond(\mathbb{J}_f) * \frac{\|\delta N\|}{\|N\|} \quad (4.9)$$

A large condition number means these errors are magnified more. The condition number can be used as a figure of merit to evaluate the geometry of the hex sensor. For the rotationally symmetric prototype hex sensor, the condition number was 2.9.

The condition number depended on several design parameters that are noted in Figure 2-6. These design parameters can be varied to minimize the condition number.

Table 4.2: Effect of varying design parameters on $cond(\mathbb{J}_f)$.

Design Parameter	Effect on $cond(\mathbb{J}_f)$
β	Increases with increasing β
θ	Minimum at $\theta = 36^\circ$
a	Increases with increasing a
D_b	Minimum at $D_b = 8\text{cm}$

Chapter 5

Preliminary Work on Full-Size Hex Sensor

Next, the learnings from the small hex sensor were applied to the full-size hex sensor (FSHS) that will connect the XRL to the worker via the harness.

5.1 Harness Selection

The XRL will be mounted to a vertical platform; the FSHS will connect the platform and the harness worn by the worker. The harness should comfortably hold the worker in the sitting and mantis positions. A rescue harness was chosen for its ability to support the wearer in multiple directions. The hex sensor design requires that the sensor be attached to the harness in three places: either with two connections at the shoulders and one at the lower back, or two at the hips and one at the upper back. Through tests it was found that the former—two shoulder connections and one lumbar connection—was the most comfortable. Figure 5-1 shows a rescue harness with the attachments in this configuration.

The Yates Voyager 380 rescue harness was chosen for its D-ring location.

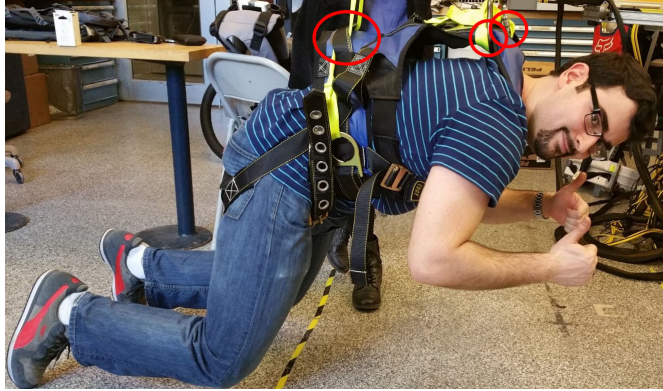


Figure 5-1: To test rescue harness comfort, a subject was suspended from the ceiling by three attachment points (circled in red) and comfort—especially how the harness dug into the subject's body—was noted.



Figure 5-2: The Yates Voyager 380 rescue harness

5.2 Joint Design

The FSHS differs from the smaller version in that the legs could only be connected to the worker's harness at three points instead of six points. The harness's included D-rings allow movement with six degrees of freedom, so they were approximated as three ball joints. A typical D-ring is shown in Figure 5-3.

Using Equation 2.1 again, we must constrain 42 degrees of freedom. This time, $P_3 = 3$ represents our 3 ball joint attachments. There are 33 degrees of freedom left, or 11 degrees of freedom per pair of legs. Figure 5-4 shows some possible joint



Figure 5-3: A typical D-ring on a rescue harness. The D-ring has three degrees of freedom and can be approximated as a ball joint.

combinations to reach this constraint. Two ball joints and a pin joint were chosen. Note that the 11 degrees of freedom per pair of legs made it impossible to have a symmetric set of joints.

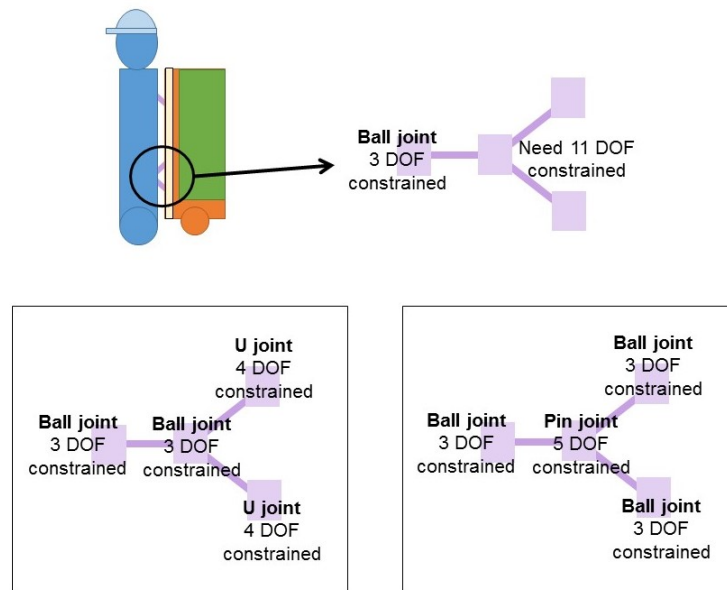


Figure 5-4: Each pair of legs needs to constrain a total of 14 degrees of freedom, and the ball joint from the harness attachment point constrained three of these. Two options for joint combinations are displayed; the ball joint and pin joint combination was chosen.

5.3 Geometry Optimization

Similar to the small hex sensor, the FSHS has a transformation matrix that turns the axial forces in each leg into the force/torque output. The design parameters for the FSHS are the attachment locations on the XRL (the attachment locations on the

harness are predetermined by the D-ring locations). Figure 5-5 shows the parameters varied.

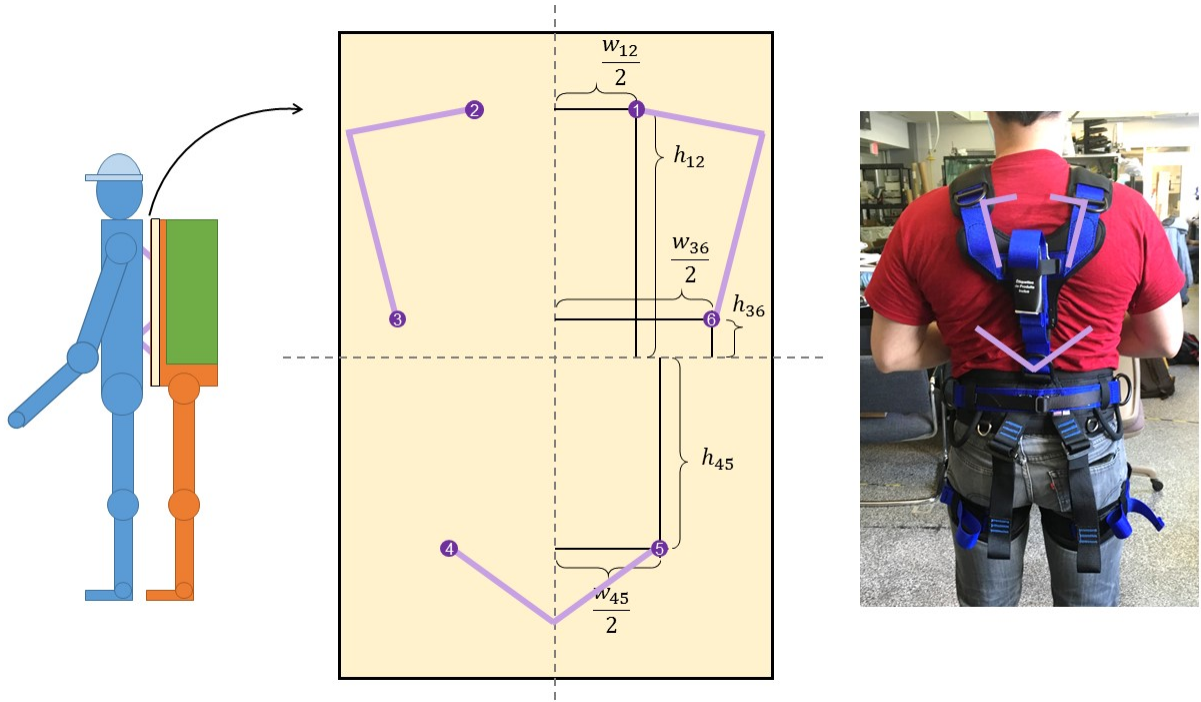


Figure 5-5: The six attachment points of each triangular pair of FSHS legs on the XRL platform were the design parameters varied in the search for the lowest condition number.

The axial forces are again read in as N :

$$N = \left(N_1 \quad N_2 \quad N_3 \quad N_4 \quad N_5 \quad N_6 \right)^T \quad (5.1)$$

First, the axial forces in each leg are broken down into their x , y , and z components (shown in Figure 5-6) in the global coordinate system by the transformation matrix \mathbb{H}_1 .

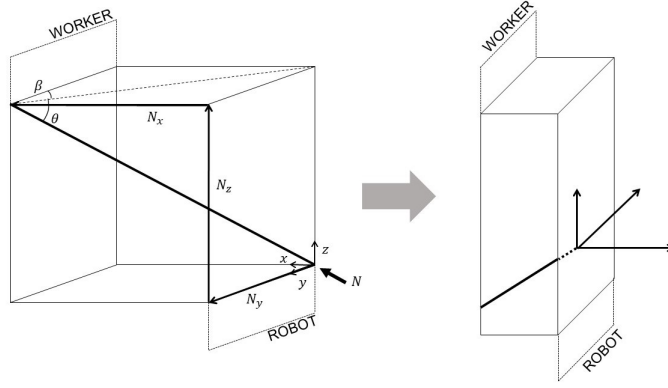


Figure 5-6: \mathbb{H}_1 breaks down axial forces into their x , y , and z components.

$$\mathbb{H}_1 = \begin{bmatrix} \cos(\theta_{12}) \sin(\beta_{12}) & 0 & 0 & 0 & 0 & 0 \\ -\cos(\theta_{12}) \cos(\beta_{12}) & 0 & 0 & 0 & 0 & 0 \\ \sin(\theta_{12}) & 0 & 0 & 0 & 0 & 0 \\ 0 \cos(\theta_{12}) \sin(\beta_{12}) & 0 & 0 & 0 & 0 & 0 \\ 0 \cos(\theta_{12}) \cos(\beta_{12}) & 0 & 0 & 0 & 0 & 0 \\ 0 \sin(\theta_{12}) & 0 & 0 & 0 & 0 & 0 \\ 0 & 0 \cos(\theta_{36}) \sin(\beta_{36}) & 0 & 0 & 0 & 0 \\ 0 & 0 \cos(\theta_{36}) \cos(\beta_{36}) & 0 & 0 & 0 & 0 \\ 0 & 0 \sin(\theta_{36}) & 0 & 0 & 0 & 0 \\ 0 & 0 & 0 \cos(\theta_{36}) \sin(\beta_{36}) & 0 & 0 & 0 \\ 0 & 0 & 0 \cos(\theta_{36}) \cos(\beta_{36}) & 0 & 0 & 0 \\ 0 & 0 & 0 \sin(\theta_{36}) & 0 & 0 & 0 \\ 0 & 0 & 0 & 0 \cos(\theta_{45}) \sin(\beta_{45}) & 0 & 0 \\ 0 & 0 & 0 & 0 \cos(\theta_{45}) \cos(\beta_{45}) & 0 & 0 \\ 0 & 0 & 0 & 0 \sin(\theta_{45}) & 0 & 0 \\ 0 & 0 & 0 & 0 & 0 \cos(\theta_{45}) \sin(\beta_{45}) & 0 \\ 0 & 0 & 0 & 0 & 0 \cos(\theta_{45}) \cos(\beta_{45}) & 0 \\ 0 & 0 & 0 & 0 & 0 \sin(\theta_{45}) & 0 \end{bmatrix} \quad (5.2)$$

$$F = \mathbb{H}_1 N \quad (5.3)$$

where

$$F = (F_{x1} \ F_{y1} \ F_{z1} \ F_{x2} \ F_{y2} \ F_{z2} \ F_{x3} \ F_{y3} \ F_{z3} \ F_{x4} \ F_{y4} \ F_{z4} \ F_{x5} \ F_{y5} \ F_{z5} \ F_{x6} \ F_{y6} \ F_{z6})^T. \quad (5.4)$$

Next, the x , y , and z components are combined to give the forces and torques applied at the center through the transformation matrix \mathbb{H}_2 .

$$\mathbb{H}_2 = \begin{bmatrix} 1 & 0 & 0 & 1 & 0 & 0 & 1 & 0 & 0 & 1 & 0 & 0 & 1 & 0 & 0 & 1 & 0 & 0 \\ 0 & 1 & 0 & 0 & 1 & 0 & 0 & 1 & 0 & 0 & 1 & 0 & 0 & 1 & 0 & 0 & 1 & 0 \\ 0 & 0 & 1 & 0 & 0 & 1 & 0 & 0 & 1 & 0 & 0 & 1 & 0 & 0 & 1 & 0 & 0 & 1 \\ 0 & 0 & \frac{w_{12}}{2} & 0 & 0 & -\frac{w_{12}}{2} & 0 & 0 & -\frac{w_{36}}{2} & 0 & 0 & -\frac{w_{45}}{2} & 0 & 0 & \frac{w_{45}}{2} & 0 & 0 & \frac{w_{36}}{2} \\ \frac{h_{12}}{2} & 0 & 0 & \frac{h_{12}}{2} & 0 & 0 & \frac{h_{36}}{2} & 0 & 0 & \frac{h_{-45}}{2} & 0 & 0 & \frac{h_{-45}}{2} & 0 & 0 & \frac{h_{36}}{2} & 0 & 0 \\ -\frac{w_{12}}{2} & 0 & 0 & \frac{w_{12}}{2} & 0 & 0 & \frac{w_{36}}{2} & 0 & 0 & \frac{w_{45}}{2} & 0 & 0 & -\frac{w_{45}}{2} & 0 & 0 & -\frac{w_{36}}{2} & 0 & 0 \end{bmatrix}. \quad (5.5)$$

$$L = \mathbb{H}_2 F \quad (5.6)$$

where

$$L = \left(L_x \quad L_y \quad L_z \quad M_x \quad M_y \quad M_z \right)^T. \quad (5.7)$$

\mathbb{H}_{norm} is found in the same way as Equation 4.4. In this case, $F_{max} = 2559\text{N}$ and $M_{max} = 21597\text{N-m}$. The total transformation matrix is then

$$\mathbb{H} = \mathbb{H}_{norm} \mathbb{H}_2 \mathbb{H}_1 \quad (5.8)$$

The condition number of \mathbb{H} is the figure of merit to optimize. Attachment distances were varied within a physically reasonable range on the XRL platform and a simple hill-climbing algorithm was used to minimize the condition number, which was 6.4. Figure 5-7 is an example plot of the condition number as h_{12} was varied.

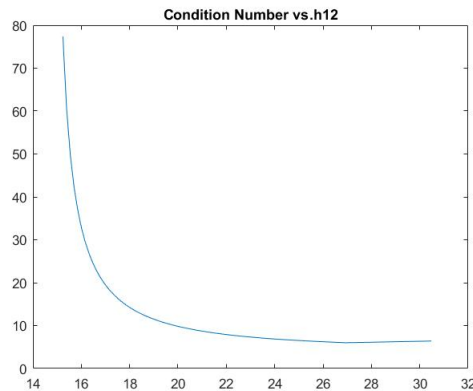


Figure 5-7: Example plot of condition number; used as part of hill-climbing minimization.

Figure 5-8 shows the final optimized geometry of the FSHS.

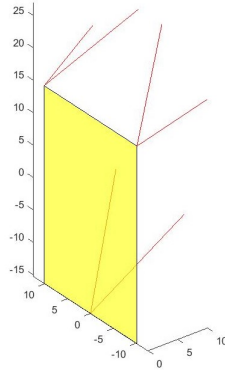


Figure 5-8: Diagram of optimal FSHS geometry

5.4 Solid Model of Full Scale Hex Sensor

A solid model was built with the dimensions obtained from optimization and the joint design discussed previously. Rod ends were used as the ball joints, and the legs were made from hollow metal tubes held in compression over threaded rods for added stiffness.

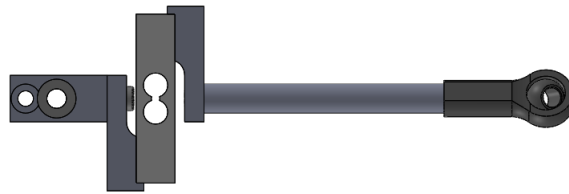


Figure 5-9: Leg design

Each pair of legs was fastened to the D-ring with a pin joint. The rod ends will be attached to the vertical XRL platform with solid gussets.

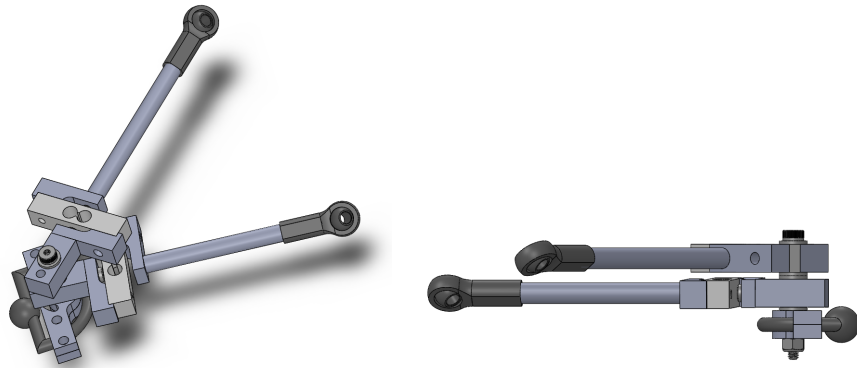


Figure 5-10: Pair of legs

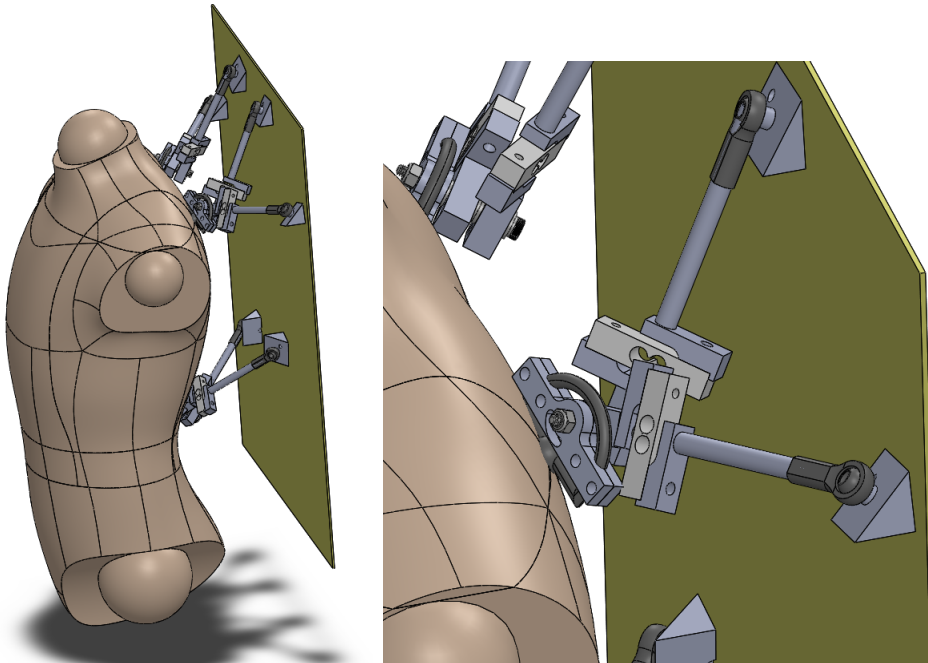


Figure 5-11: Solid model of proposed full-size hex sensor

Chapter 6

Conclusions and Future Work

This work presents the design and analysis of a prototype hexapod-based multiaxis force sensor with a geometry that allows it to be used as both a load cell and attachment between extra robot limbs and their human operator. A figure of merit, the condition number, is used to compare the effectiveness of different geometries. A full-scale hex sensor (FSHS) is then designed using the condition number to guide the geometry.

The small hex sensor will be used to implement real-time force sensing, and combined with a small-scale set of XRL to create a prototype human follower. However, most future work will focus on the FSHS. The effect of attaching the FSHS to a compliant harness instead of a rigid platform will be studied, especially the possible movement of the attachment points due to the stretchiness of the fabric and the resulting loss of accuracy of the measured forces. The compliant harness will also act as a spring, introducing a resonant frequency than can be pinpointed with a Fourier transform. The design may need to be altered to ensure the resonant frequency is higher than typical walking frequencies. Finally, safety features must be considered for situations in which the XRL motors fail and the worker is left carrying the weight of the XRL by himself, or in which the worker slips and applies a sudden force on the sensors. Possible harness alterations to protect the worker in case of motor failure include load lifters like those found on hiking backpacks that can be tightened in case of an emergency to transfer the weight of the XRL from the shoulders to the waist

of the worker. Another idea is a mechanism similar to the Second Spine developed by the Center for Composite Materials at the University of Delaware, which can be either compliant or stiff to transfer loads to the hips [5]. Extra robotic limbs have the potential to improve the experience of hazardous site workers while saving time and money, and the hex sensor will be a vital safety feature.



Figure 6-1: Load lifters are common hiking pack features that transfer weight from the shoulders to the hips.

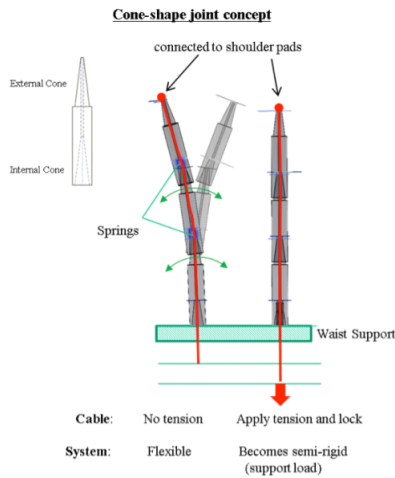


Figure 6-2: The Second Spine can either be loose and flexible, or, when, pulled into compression, rigid and load-bearing.

Bibliography

- [1] Nuclear Power Plant Outages No Place for Cowboys, November 25 2013.
- [2] Tim Bonfield. Hazmat training reveals dangers, November 19 2001.
- [3] Stephen Boyd. Svd applications. University Lecture, 2007.
- [4] Ashitava Ghosal. Six component force-torque sensors using gough-stewart platform manipulators. 2010.
- [5] Park J, Stegall P, Zanutto D, Vashista V, Jin X, and Agrawal SK. Design of the second spine: A secondary pathway to transfer loads from the shoulders to the pelvis. In *2013 Proceedings of the ASME International Design Engineering Technical Conferences and Computers and Information in Engineering Conference, DETC2013*, volume 6 PART B, 2013.
- [6] Aaron Sheldrick and Minami Funakoshi. Fukushima’s ground zero: No place for man or robot, March 2016.
- [7] Eliza Strickland. Meet the Robots of Fukushima Daiichi, February 28 2014.
- [8] Masaru Uchiyama, Yoshihiro Nakamura, and Kyojiro Hakomori. Evaluation of the robot force sensor structure using singular value decomposition. *Advanced Robotics*, 5(1):39–52, 1990.